JOURNAL OF MODERN OPTICS
https://doi.org/10.1080/09500340.2019.1605005

Taylor & Francis
Taylor & Francis Group

A light scattering model for total internal reflection microscopy of geometrically anisotropic particles

Adrian Doicu[a], Alina A. Vasilyeva[b], Dmitry S. Efremenko[a], Christopher L. Wirth[c] and Thomas Wriedt[d]

[a]Deutsches Zentrums für Luft- und Raumfahrt (DLR), Institut of Remote Sensing, Oberpfaffenhofen, Germany; [b]Faculty of Electrical Engineering and Information Technology, University of Applied Sciences Rosenheim, Rosenheim, Germany; [c]Chemical and Biomedical Engineering Department, Cleveland State University, Cleveland, OH, USA; [d]Leibniz-Institut für Werkstofforientierte Technologien – IWT, University of Bremen, Bremen, Germany

ABSTRACT

In this paper, a light scattering model for Total Internal Reflection Microscopy (TIRM) is described. The model handles the scattering by an axisymmetric particle of arbitrary orientation situated in the evanescent field near a plane surface, and the imaging of the scattered light via microscope optics. The scattering problem is solved by using the T-matrix method and the rotation addition theorem for spherical vector wave functions, while the image of the scattered field is computed by using the Debye diffraction integral. The numerical simulations provide evidence of two working regimes for TIRM: the first regime, corresponding to an incident angle less than the critical angle of total internal reflection, provides information on the size and the orientation of the particle, while the second regime, corresponding to an incident angle larger than the critical angle of total internal reflection, is recommended for measuring the distance between the particle and plane surface.

ARTICLE HISTORY
Received 11 December 2018
Accepted 31 March 2019

KEYWORDS
Total internal reflection microscopy; light scattering model; T-matrix

1. Introduction

Total Internal Reflection Microscopy (TIRM) has proven to be an effective technique to measure weak interaction forces between spherical colloidal particles and surfaces with a resolution of a few femtonewton [1]. In an experimental setup a laser beam is coupled into a prism and hits the glass-water interface with an angle slightly above the critical angle of total internal reflection. This generates an evanescent field near the interface that decays in the lower refractive index medium (water) with a characteristic penetration depth which depends on the angle of incidence. A colloidal particle that is dispersed in the medium will scatter light from the evanescent field if it is in the vicinity of the surface. TIRM has proven to be a valuable tool for the precise measurement of weak colloidal interactions such as double layer forces [2,3], van der Waals forces [4,5], electrically mediated interactions [6,7], polymer mediated steric repulsion [8,9], and depletion forces [10,11]. An exhaustive review on TIRM can be found in [12,13].

To design a TIRM instrument for a specific measuring problem, a light scattering model is needed. Essentially, we have to model the scattering by an axisymmetric particle of arbitrary orientation situated near a plane surface, and the imaging of the scattered light through an optical system. Either a photomultiplier tube that automatically integrates the scattered light signal or a digital camera that collects an image of the scattering [13], which is then integrated, are used to conduct TIRM. As the scattering problem is a multiple scattering problem, the separation of variables technique is a highly suitable simulation approach. The approach based on the T-Matrix method was originally developed by Helden et al. [14], and it has been validated by comparing the measurements [15].

To model the scattering problem in the framework of the separation of variables technique, one must address how the radiation interacts with the particle and with the plane interface. The incident field strikes the particle directly, while the fields emanating from the particle may reflect off the surface and interact with the particle again. The transition matrix relating the incident and scattered field coefficients is computed in the framework of the T-matrix method, and the reflection matrix characterizing the reflection of the scattered field by the surface is computed by using the integral representation for the spherical vector wave functions. To handle an arbitrary particle orientation, we will use the rotation addition theorem for spherical vector wave functions.

CONTACT Thomas Wriedt thw@iwt.uni-bremen.de Leibniz-Institut fürWerkstofforientierte Technologien – IWT, University of Bremen, Bremen, Germany

Essentially, this theorem will enable us to pass from the field expansions in the global coordinate system to the field expansions in the particle coordinate system and vice versa. In general, if the particle coordinate system $O_o x_p y_p z_p$ is obtained by rotating the global coordinate system $O_o x_o y_o z_o$ thought the Euler angles $(\alpha_p, \beta_p, \gamma_p)$, the rotation addition theorem for spherical vector wave functions is [16]

$$\mathbf{M}_{mn}^{1,3}(kr,\theta,\varphi) = \sum_{m'=-n}^{n} D_{mm'}^{n}(\alpha_p,\beta_p,\gamma_p)\mathbf{M}_{m'n}^{1,3}(kr,\theta_p,\varphi_p), \tag{1}$$

$$\mathbf{N}_{mn}^{1,3}(kr,\theta,\varphi) = \sum_{m'=-n}^{n} D_{mm'}^{n}(\alpha_p,\beta_p,\gamma_p)\mathbf{N}_{m'n}^{1,3}(kr,\theta_p,\varphi_p), \tag{2}$$

where $D_{mm'}^{n}$ are the Wigner D-functions, (r,θ,φ) are the spherical coordinates of a field point in the global coordinate system, and (r,θ_p,φ_p) are the spherical coordinates of the same field point in the particle coordinate system. A direct consequence of the arbitrary particle orientation is that the scattering problem will not decouple over the azimuthal modes as it happens when the axis of symmetry of the particle is perpendicular to the plane surface [17].

As an imaging system, we consider pairs of lenses arranged in a 4f configuration, that is to say they are placed such that their foci coincide, for both illumination and image formation. The particle is placed in the front focal plane of the first lens, such that a corresponding image field results in the back focal plane of the second lens in a phase correct manner. Critically, the aperture stop is placed in the common focal plane of the lens pair, yielding an afocal and telecentric system from both object and image spaces.

The next parts of the paper are organized as follows. In Section 2, we present the mathematical model of TIRM dealing with scattering by an axisymmetric particle of arbitrary orientation situated near a plane surface, followed by imaging of the scattered light. A numerical analysis of the TIRM model is the objective of Section 3, while conclusions are formulated in Section 4.

2. Theory

The geometry of the scattering problem and the imaging system are shown in Figure 1. An axisymmetric particle of arbitrary orientation is situated in the neighbourhood of a plane surface Σ. The imaging system is represented by the two sections of the Gaussian reference spheres of the collector and detector lens, P_o and P_i, respectively. Let $O_o x_o y_o z_o$ be a coordinate system centred at the particle, and in this way at the focal point of the collector lens, and $O_i x_i y_i z_i$ a coordinate system centred at the focal point of the detector lens. In the (global) coordinate system $O_o x_o y_o z_o$, the axial position of the plane surface Σ, which is perpendicular to the z_o-axis, is specified by the distance z_0, and we have $z_0 = d + R$, where R is the radius of the sphere circumscribing the particle and d is the effective distance between the particle and the plane surface (i.e. the distance between the plane surface and the circumscribing sphere). Moreover, in the coordinate system $O_o x_o y_o z_o$, let the orientation of the particle be described by the Euler orientation angles (α_p, β_p). The refractive index of the particle is n_p, the refractive index of the substrate is n_s, and the refractive indices in the object space (ambient medium) and the image space are n_o and n_i, respectively. The focal lengths of the collector and detector lens are f_o and f_i, respectively.

2.1. Scattering by the particle near the substrate

The incident field is a linearly polarized vector plane wave propagating in the glass substrate and is given by

$$\mathbf{E}_0(\mathbf{r}) = (E_{0\beta}\mathbf{e}_\beta + E_{0\alpha}\mathbf{e}_\alpha)e^{j\mathbf{k}_s\cdot\mathbf{r}}. \tag{3}$$

The incident wave vector $\mathbf{k}_s = k_s\mathbf{e}_k$, where $k_s = k_0 n_s$ is the wavenumber in the substrate, k_0 is the wavenumber in free space, and $(\mathbf{e}_k, \mathbf{e}_\beta, \mathbf{e}_\alpha)$ are the spherical unit vectors associated with $\mathbf{k}_s$, is assumed to be in the $x_o z_o$-plane and to enclose the angle β_s with the z_o-axis. The vector plane wave transmitted (or refracted) into the ambient medium is

$$\mathbf{E}_0^{\mathrm{T}}(\mathbf{r}) = (E_{0\beta}^{\mathrm{T}}\mathbf{e}_{\beta\mathrm{T}} + E_{0\alpha}^{\mathrm{T}}\mathbf{e}_{\alpha\mathrm{T}})e^{j\mathbf{k}_o\cdot\mathbf{r}}, \tag{4}$$

where

$$E_{0\beta}^{\mathrm{T}} = t_\parallel(\beta_s)e^{jk_o z_0(\cos\beta - m_{rs}\cos\beta_s)}E_{0\beta}, \tag{5}$$

$$E_{0\alpha}^{\mathrm{T}} = t_\perp(\beta_s)e^{jk_o z_0(\cos\beta - m_{rs}\cos\beta_s)}E_{0\alpha}, \tag{6}$$

$\mathbf{k}_o = k_o\mathbf{e}_{k\mathrm{T}}$ is the transmitted wave vector, $k_o = k_0 n_o$ is the wavenumber in the ambient medium, $m_{rs} = n_s/n_o$ is the relative refractive index of the substrate with respect to the ambient medium, and $(\mathbf{e}_{k\mathrm{T}}, \mathbf{e}_{\beta\mathrm{T}}, \mathbf{e}_{\alpha\mathrm{T}})$ are the spherical unit vectors associated with $\mathbf{k}_o$. The Fresnel transmission coefficients are given by

$$t_\parallel(\beta_s) = \frac{2m_{rs}\cos\beta_s}{\cos\beta_s + m_{rs}\cos\beta}, \tag{7}$$

$$t_\perp(\beta_s) = \frac{2m_{rs}\cos\beta_s}{m_{rs}\cos\beta_s + \cos\beta}, \tag{8}$$

while the angle of refraction is computed by means of Snell's law:

$$\sin\beta = m_{rs}\sin\beta_s, \tag{9}$$

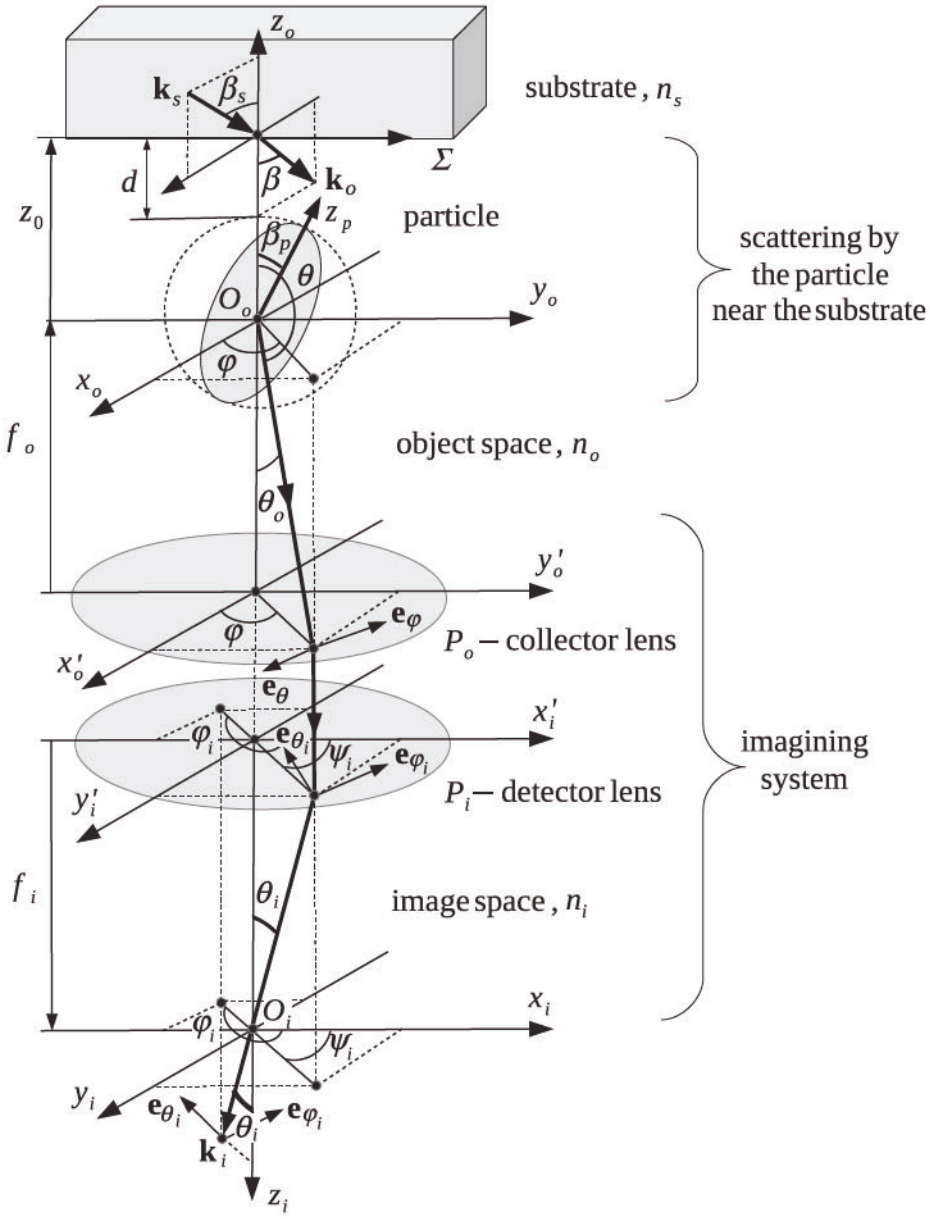

Figure 1. Geometry of the scattering problem and the imaging system.

$$\cos\beta = \pm\sqrt{1-\sin^2\beta}. \tag{10}$$

Evanescent waves appear for real m_{rs} and incident angles $\beta_s > \beta_{sc}$, where $\beta_{sc} = \arcsin(1/m_{rs})$ is the angle of total internal reflection. In this case, $\sin\beta > 1$ and $\cos\beta$ is purely imaginary. For $\mathbf{r} = (x_o, y_o, z_o)$ and negative values of z_o, we have

$$\exp(j\mathbf{k}_o \cdot \mathbf{r}) = \exp(jk_o|z_o|\cos\beta + jk_o x_o \sin\beta),$$

and we choose the sign of the square root such that $\mathrm{Im}(\cos\beta) > 0$. This choice guarantees that the amplitude of the refracted wave propagating in the negative direction of the z_o-axis decreases with increasing the distance $|z_o|$. In the global and particle coordinate systems, the transmitted incident fields can be expanded in terms of regular spherical vector wave functions, that is,

$$\begin{aligned}\mathbf{E}_0^{\mathrm{T}}(\mathbf{r}) &= \sum_{n=1}^{\infty}\sum_{m=-n}^{n} A_{mn}^{\mathrm{T}}\mathbf{M}_{mn}^{1}(k_o r,\theta,\varphi) \\ &\quad + B_{mn}^{\mathrm{T}}\mathbf{N}_{mn}^{1}(k_o r,\theta,\varphi) \\ &= \sum_{n=1}^{\infty}\sum_{m=-n}^{n} a_{mn}^{\mathrm{T}}\mathbf{M}_{mn}^{1}(k_o r,\theta_p,\varphi_p) \\ &\quad + b_{mn}^{\mathrm{T}}\mathbf{N}_{mn}^{1}(k_o r,\theta_p,\varphi_p),\end{aligned} \tag{11}$$

where (r,θ,φ) are the spherical coordinates of a field point in the global coordinate system $O_o x_o y_o z_o$, (r,θ_p,φ_p) are the spherical coordinates of the same field

point in the particle coordinate system $O_o x_p y_p z_p$,

$$A_{mn}^{T} = -\frac{4j^n}{\sqrt{2n(n+1)}}[jm\pi_n^{|m|}(\beta)\,E_{0\beta}^{T} + \tau_n^{|m|}(\beta)\,E_{0\alpha}^{T}], \tag{12}$$

$$B_{mn}^{T} = -\frac{4j^{n+1}}{\sqrt{2n(n+1)}}[\tau_n^{|m|}(\beta)\,E_{0\beta}^{T} - jm\pi_n^{|m|}(\beta)\,E_{0\alpha}^{T}], \tag{13}$$

and

$$a_{m'n}^{T} = \sum_{m=-n}^{n} A_{mn}^{T} D_{mm'}^{n}(\alpha_p, \beta_p, 0), \tag{14}$$

$$b_{m'n}^{T} = \sum_{m=-n}^{n} B_{mn}^{T} D_{mm'}^{n}(\alpha_p, \beta_p, 0). \tag{15}$$

Similarly, in the global and particle coordinate systems, the scattered field is expanded in terms of radiating spherical vector wave functions:

$$\begin{aligned}\mathbf{E}_{sct}(\mathbf{r}) &= \sum_{n=1}^{\infty}\sum_{m=-n}^{n} F_{mn}\mathbf{M}_{mn}^{3}(k_o r,\theta,\varphi) \\ &\quad + G_{mn}\mathbf{N}_{mn}^{3}(k_o r,\theta,\varphi) \\ &= \sum_{n=1}^{\infty}\sum_{m=-n}^{n} f_{mn}\mathbf{M}_{mn}^{3}(k_o r,\theta_p,\varphi_p) \\ &\quad + g_{mn}\mathbf{N}_{mn}^{3}(k_o r,\theta_p,\varphi_p),\end{aligned} \tag{16}$$

where

$$F_{m'n} = \sum_{m=-n}^{n} f_{mn} D_{mm'}^{n}(0, -\beta_p, \alpha_p), \tag{17}$$

$$G_{m'n} = \sum_{m=-n}^{n} g_{mn} D_{mm'}^{n}(0, -\beta_p, \alpha_p). \tag{18}$$

In addition to the fields described by Equations (11) and (16), a third field exists in the ambient medium. This field is called the interacting field, and it is the result of the scattered field reflecting off the surface and striking the particle. In the global coordinate system, the interacting field can be expressed as

$$\begin{aligned}\mathbf{E}_{sct}^{R}(\mathbf{r}) &= \sum_{n=1}^{\infty}\sum_{m=-n}^{n} F_{mn}\mathbf{M}_{mn}^{3R}(k_o r,\theta,\varphi) \\ &\quad + G_{mn}\mathbf{N}_{mn}^{3R}(k_o r,\theta,\varphi),\end{aligned} \tag{19}$$

where $\mathbf{M}_{mn}^{3R}(k_o r,\theta,\varphi)$ and $\mathbf{N}_{mn}^{3R}(k_o r,\theta,\varphi)$ are the radiating spherical vector wave functions reflected by the plane surface. For $\mathbf{r}$ inside a sphere enclosed in the particle and a given azimuthal mode m, the reflected spherical vector wave functions can be expanded as

$$\begin{aligned}\begin{pmatrix}\mathbf{M}_{mn}^{3R}(k_o r,\theta,\varphi)\\ \mathbf{N}_{mn}^{3R}(k_o r,\theta,\varphi)\end{pmatrix} &= \sum_{n'=1}^{\infty}\begin{pmatrix}\alpha_{mnn'}\\ \gamma_{mnn'}\end{pmatrix}\mathbf{M}_{mn'}^{1}(k_o r,\theta,\varphi) \\ &\quad + \begin{pmatrix}\beta_{mnn'}\\ \delta_{mnn'}\end{pmatrix}\mathbf{N}_{mn'}^{1}(k_o r,\theta,\varphi),\end{aligned} \tag{20}$$

whence inserting Equation (20) into Equation (19), we obtain the following series representation for the interacting field in terms of regular spherical vector wave functions:

$$\begin{aligned}\mathbf{E}_{sct}^{R}(\mathbf{r}) &= \sum_{n'=1}^{\infty}\sum_{m=-n'}^{n'} F_{mn'}^{R}\mathbf{M}_{mn'}^{1}(k_o r,\theta,\varphi) \\ &\quad + G_{mn'}^{R}\mathbf{N}_{mn'}^{1}(k_o r,\theta,\varphi),\end{aligned} \tag{21}$$

where

$$\begin{pmatrix}F_{mn'}^{R}\\ G_{mn'}^{R}\end{pmatrix} = \sum_{n=1}^{\infty}\begin{pmatrix}\alpha_{mnn'}\\ \beta_{mnn'}\end{pmatrix}F_{mn} + \begin{pmatrix}\gamma_{mnn'}\\ \delta_{mnn'}\end{pmatrix}G_{mn}. \tag{22}$$

In [17], the expressions of the expansion coefficients $\alpha_{mnn'}$, $\beta_{mnn'}$, $\gamma_{mnn'}$ and $\delta_{mnn'}$ have been derived by making use of the integral representation of the radiating spherical vector wave functions; the results are

$$\begin{aligned}\alpha_{mnn'} &= \frac{2j^{n'-n}}{\sqrt{nn'(n+1)(n'+1)}}\int_0^{\pi/2-j\infty} \\ &\quad \times [m^2\pi_n^{|m|}(\beta)\pi_{n'}^{|m|}(\pi-\beta)r_{\parallel}(\beta) \\ &\quad + \tau_n^{|m|}(\beta)\tau_{n'}^{|m|}(\pi-\beta)r_{\perp}(\beta)]e^{2jk_o z_0\cos\beta}\sin\beta\,d\beta,\end{aligned} \tag{23}$$

$$\begin{aligned}\beta_{mnn'} &= \frac{2j^{n'-n}}{\sqrt{nn'(n+1)(n'+1)}}\int_0^{\pi/2-j\infty} \\ &\quad \times m[\pi_n^{|m|}(\beta)\tau_{n'}^{|m|}(\pi-\beta)r_{\parallel}(\beta) \\ &\quad + \tau_n^{|m|}(\beta)\pi_{n'}^{|m|}(\pi-\beta)r_{\perp}(\beta)]e^{2jk_0 z_0\cos\beta}\sin\beta\,d\beta,\end{aligned} \tag{24}$$

$$\begin{aligned}\gamma_{mnn'} &= \frac{2j^{n'-n}}{\sqrt{nn'(n+1)(n'+1)}}\int_0^{\pi/2-j\infty} \\ &\quad \times m[\tau_n^{|m|}(\beta)\pi_{n'}^{|m|}(\pi-\beta)r_{\parallel}(\beta) \\ &\quad + \pi_n^{|m|}(\beta)\tau_{n'}^{|m|}(\pi-\beta)r_{\perp}(\beta)]e^{2jk_o z_0\cos\beta}\sin\beta\,d\beta,\end{aligned} \tag{25}$$

$$\begin{aligned}\delta_{mnn'} &= \frac{2j^{n'-n}}{\sqrt{nn'(n+1)(n'+1)}}\int_0^{\pi/2-j\infty} \\ &\quad \times [\tau_n^{|m|}(\beta)\tau_{n'}^{|m|}(\pi-\beta)r_{\parallel}(\beta)\end{aligned}$$

$$+ m^2 \pi_n^{|m|}(\beta)\pi_{n'}^{|m|}(\pi-\beta) r_\perp(\beta)]$$
$$\times e^{2jk_o z_0 \cos\beta} \sin\beta \mathrm{d}\beta. \quad (26)$$

Note that the integrals in Equations (23)–(26) are of the form

$$I = \int_0^{\pi/2-j\infty} f(\cos\beta) e^{2jq\cos\beta} \sin\beta \mathrm{d}\beta.$$

By changing variables from β to $x = -2jq(\cos\beta - 1)$, we are led to the integrals

$$I = \frac{e^{2jq}}{2jq} \int_0^\infty f\left(1 - \frac{x}{2jq}\right) e^{-x} \mathrm{d}x,$$

which can be computed efficiently by using the Laguerre polynomials. In the particle coordinate system, the expansion of the interacting field reads as

$$\mathbf{E}^{\mathrm{R}}_{\mathtt{sct}}(\mathbf{r}) = \sum_{n'=1}^{\infty} \sum_{m=-n'}^{n'} f^{\mathrm{R}}_{mn'} \mathbf{M}^1_{mn'}(k_o r, \theta_p, \varphi_p) + g^{\mathrm{R}}_{mn'} \mathbf{N}^1_{mn'}(k_o r, \theta_p, \varphi_p), \quad (27)$$

with

$$f^{\mathrm{R}}_{m'n} = \sum_{m=-n}^{n} F^{\mathrm{R}}_{mn} D^n_{mm'}(\alpha_p, \beta_p, 0), \quad (28)$$

$$g^{\mathrm{R}}_{m'n} = \sum_{m=-n}^{n} G^{\mathrm{R}}_{mn} D^n_{mm'}(\alpha_p, \beta_p, 0). \quad (29)$$

Then, accounting of Equations (17), (18), (22), (28), and (29), we obtain the following representations of f^{R}_{mn} and g^{R}_{mn} in terms of f_{mn} and g_{mn}:

$$f^{\mathrm{R}}_{m'n'} = \sum_{n=1}^{\infty} \sum_{m=-n}^{n} \left\{ \left[\sum_{m''=-n'}^{n'} \alpha_{m''nn'} D^n_{mm''}(0, -\beta_p, \alpha_p) \times D^{n'}_{m''m'}(\alpha_p, \beta_p, 0) \right] f_{mn} + \left[\sum_{m''=-n'}^{n'} \gamma_{m''nn'} D^n_{mm''}(0, -\beta_p, \alpha_p) \times D^{n'}_{m''m'}(\alpha_p, \beta_p, 0) \right] g_{mn} \right\}, \quad (30)$$

$$g^{\mathrm{R}}_{m'n'} = \sum_{n=1}^{\infty} \sum_{m=-n}^{n} \left\{ \left[\sum_{m''=-n'}^{n'} \beta_{m''nn'} D^n_{mm''}(0, -\beta_p, \alpha_p) \times D^{n'}_{m''m'}(\alpha_p, \beta_p, 0) \right] f_{mn} + \left[\sum_{m''=-n'}^{n'} \delta_{m''nn'} D^n_{mm''}(0, -\beta_p, \alpha_p) \times D^{n'}_{m''m'}(\alpha_p, \beta_p, 0) \right] g_{mn} \right\}. \quad (31)$$

In the particle coordinate system, the scattered field coefficients are related to the expansion coefficients of the fields striking the particle through the transition matrix T. Truncating the expansions given by Equations (11), (16) and (21), we find the following matrix equation:

$$\begin{bmatrix} f_{mn} \\ g_{mn} \end{bmatrix} = [T_{mn,m'n'}] \left(\begin{bmatrix} a^{\mathrm{T}}_{m'n'} \\ b^{\mathrm{T}}_{m'n'} \end{bmatrix} + \begin{bmatrix} f^{\mathrm{R}}_{m'n'} \\ g^{\mathrm{R}}_{m'n'} \end{bmatrix} \right). \quad (32)$$

Here, n and n' range from 1 to N_{rank}, while m and m' range from $-M_{\mathrm{rank}}$ to M_{rank}, with N_{rank} and M_{rank} being the maximum expansion and azimuthal orders, respectively. In the particle coordinate system, the expansion coefficients of the interacting field are related to the scattered field coefficients by the so-called reflection matrix:

$$\begin{bmatrix} f^{\mathrm{R}}_{m'n'} \\ g^{\mathrm{R}}_{m'n'} \end{bmatrix} = [R_{mnm'n'}] \begin{bmatrix} f_{mn} \\ g_{mn} \end{bmatrix}, \quad (33)$$

where, in view of Equations (30) and (31), we have

$$[R_{mnm'n'}] = \begin{bmatrix} \alpha_{mnm'n'} & \gamma_{mnm'n'} \\ \beta_{mnm'n'} & \delta_{mnm'n'} \end{bmatrix}, \quad (34)$$

with

$$\alpha_{mnm'n'} = \sum_{m''=-n'}^{n'} \alpha_{m''nn'} D^n_{mm''}(0, -\beta_p, \alpha_p) \times D^{n'}_{m''m'}(\alpha_p, \beta_p, 0), \quad (35)$$

and similarly for $\beta_{mnm'n'}$, $\gamma_{mnm'n'}$ and $\delta_{mnm'n'}$. Now it is apparent that the scattered field coefficients f_{mn} and g_{mn} can be obtained by combining the matrix equations (32) and (33); we get

$$\left(\mathsf{I} - [T_{mn,m'n'}][R_{mnm'n'}]\right) \begin{bmatrix} f_{mn} \\ g_{mn} \end{bmatrix} = [T_{mn,m'n'}] \begin{bmatrix} a^{\mathrm{T}}_{m'n'} \\ b^{\mathrm{T}}_{m'n'} \end{bmatrix}, \quad (36)$$

where I is the identity matrix. It should be noted that for axisymmetric particles with arbitrary orientation, the scattering problem has to be solved simultaneously for all azimuthal modes. The matrices which enter in Equation (36) are of dimension $2N_{\mathtt{max}} \times 2N_{\mathtt{max}}$, where

$$N_{\mathtt{max}} = N_{\mathtt{rank}} + M_{\mathtt{rank}}(2N_{\mathtt{rank}} - M_{\mathtt{rank}} + 1).$$

For this reason, the computer code dealing with arbitrary particle orientation is more time consuming than

the code dealing with particles having the axis of symmetry perpendicular to the plane surface. Once the scattered field coefficients in the particle coordinate system f_{mn} and g_{mn} have been computed, the scattered field coefficients in the global coordinate system F_{mn} and G_{mn} can be obtained from Equation (17).

In the far-field region, the scattered field below the plane surface ($\pi/2 < \theta < \pi$) sums the contribution of the direct electric far-field pattern $\mathbf{E}^{\mathrm{D}}_{\mathrm{s}\infty}(\theta,\varphi)$,

$$\mathbf{E}^{\mathrm{D}}_{\mathrm{s}\infty}(\theta,\varphi) = \frac{1}{k_{\mathrm{o}}}\sum_{n=1}^{\infty}\sum_{m=-n}^{n}(-\mathrm{j})^{n+1}[F_{mn}\mathbf{m}_{mn}(\theta,\varphi) + \mathrm{j}G_{mn}\mathbf{n}_{mn}(\theta,\varphi)] \tag{37}$$

and the interacting electric far-field pattern $\mathbf{E}^{\mathrm{R}}_{\mathrm{s}\infty}(\theta,\varphi)$,

$$\mathbf{E}^{\mathrm{R}}_{\mathrm{s}\infty}(\theta,\varphi) = \frac{1}{k_{\mathrm{o}}}\sum_{n=1}^{\infty}\sum_{m=-n}^{n}(-\mathrm{j})^{n+1}[F_{mn}\mathbf{m}^{\mathrm{R}}_{mn}(\theta,\varphi) + \mathrm{j}G_{mn}\mathbf{n}^{\mathrm{R}}_{mn}(\theta,\varphi)], \tag{38}$$

where $\mathbf{m}_{mn}$ and $\mathbf{n}_{mn}$ are the vector spherical harmonics, and $\mathbf{m}^{\mathrm{R}}_{mn}$ and $\mathbf{n}^{\mathrm{R}}_{mn}$ are the reflected vector spherical harmonics,

$$\mathbf{m}^{\mathrm{R}}_{mn}(\theta,\varphi) = \frac{1}{\sqrt{2n(n+1)}}\mathrm{e}^{-2\mathrm{j}k_{\mathrm{o}}z_0\cos\theta}[\mathrm{j}m\pi_n^{|m|}(\theta)r_{\parallel}(\theta)\mathbf{e}_{\theta} - \tau_n^{|m|}(\theta)r_{\perp}(\theta)\mathbf{e}_{\varphi}]\mathrm{e}^{\mathrm{j}m\varphi}, \tag{39}$$

$$\mathbf{n}^{\mathrm{R}}_{mn}(\theta,\varphi) = \frac{1}{\sqrt{2n(n+1)}}\mathrm{e}^{-2\mathrm{j}k_{\mathrm{o}}z_0\cos\theta}[\tau_n^{|m|}(\theta)r_{\parallel}(\theta)\mathbf{e}_{\theta} + \mathrm{j}m\pi_n^{|m|}(\theta)\,r_{\perp}(\theta)\mathbf{e}_{\varphi}]\mathrm{e}^{\mathrm{j}m\varphi}. \tag{40}$$

In Equations (39) and (40), $r_{\parallel}$ and $r_{\perp}$ are the Fresnel reflection coefficients given by

$$r_{\parallel}(\theta) = \frac{m_{\mathrm{rs}}\cos\theta - \cos\theta_{\mathrm{s}}}{m_{\mathrm{rs}}\cos\theta + \cos\theta_{\mathrm{s}}}, \tag{41}$$

$$r_{\perp}(\theta) = \frac{\cos\theta - m_{\mathrm{rs}}\cos\theta_{\mathrm{s}}}{\cos\theta + m_{\mathrm{rs}}\cos\theta_{\mathrm{s}}}, \tag{42}$$

with $\sin\theta_{\mathrm{s}} = (1/m_{\mathrm{rs}})\sin\theta$.

Thus, the solution of the scattering problem in the framework of the separation of variables method involves the following steps:

(1) calculation of the T matrix relating the expansion coefficients of the fields striking the particle to the scattered field coefficients;
(2) calculation of the reflection matrix R characterizing the reflection of spherical vector wave functions by the surface;
(3) computation of an approximate solution by solving matrix equation (36);
(4) computation of the far-field pattern by using (37) and (38).

2.2. Imaging of the scattered light

Calculation of the image of the scattered field involves the following steps:

(1) computation of the scattered field on the Gaussian reference sphere of the collector lens,
(2) computation of the transmitted field on the Gaussian reference sphere of the detector lens, and
(3) computation of the focus field by means of the Debye diffraction integral.

Before proceeding, we note that the aperture angles in the object and image spaces, i.e. the polar angles under which the Gaussian reference spheres are observed at the foci of the collector and detector lens, respectively, are computed as

$$\Theta_{\mathrm{o}} = \arcsin(\mathrm{NA}_{\mathrm{o}}/n_{\mathrm{o}}),$$
$$\Theta_{\mathrm{i}} = \arctan\left(\frac{f_{\mathrm{o}}}{f_{\mathrm{i}}}\tan\Theta_{\mathrm{o}}\right),$$

where NA_{o} is the numerical aperture of the collector lens and $\mathrm{NA}_{\mathrm{i}} = n_{\mathrm{i}}\sin\Theta_{\mathrm{i}}$ is the numerical aperture of the detector lens.

Step 1. The scattered field on the Gaussian reference sphere of the collector lens is given by

$$\mathbf{E}_{\mathrm{s}}(\theta,\varphi) = E_{\mathrm{s}\theta}(\theta,\varphi)\mathbf{e}_{\theta} + E_{\mathrm{s}\varphi}(\theta,\varphi)\mathbf{e}_{\varphi}, \tag{43}$$

where

$$E_{\mathrm{s}\theta}(\theta,\varphi) = \frac{\mathrm{e}^{\mathrm{j}k_{\mathrm{o}}f_{\mathrm{o}}}}{f_{\mathrm{o}}}[E^{\mathrm{D}}_{\mathrm{s}\infty\theta}(\theta,\varphi) + E^{\mathrm{R}}_{\mathrm{s}\infty\theta}(\theta,\varphi)], \tag{44}$$

$$E_{\mathrm{s}\varphi}(\theta,\varphi) = \frac{\mathrm{e}^{\mathrm{j}k_{\mathrm{o}}f_{\mathrm{o}}}}{f_{\mathrm{o}}}[E^{\mathrm{D}}_{\mathrm{s}\infty\varphi}(\theta,\varphi) + E^{\mathrm{R}}_{\mathrm{s}\infty\varphi}(\theta,\varphi)], \tag{45}$$

while the so-called integral response of the detector is computed as

$$P = f_{\mathrm{o}}^2\int_0^{2\pi}\int_0^{\Theta_{\mathrm{o}}}[|E_{\mathrm{s}\theta}(\theta,\varphi)|^2 + |E_{\mathrm{s}\varphi}(\theta,\varphi)|^2]\sin\theta\,\mathrm{d}\theta\,\mathrm{d}\varphi. \tag{46}$$

Step 2. The transmitted field in the image space can be computed by (vector) ray tracing. We assume that a ray propagating in the object space in the direction (θ,φ) is deflected into a ray that propagates in the image space in the direction $(\theta_{\mathrm{i}},\varphi_{\mathrm{i}})$, where

$$\theta_{\mathrm{i}} = \arctan[(f_{\mathrm{o}}/f_{\mathrm{i}})\tan(\theta-\pi)],$$

$$\varphi_i = \psi_i + \pi = 3\pi/2 - \varphi.$$

Consequently, the polar unit vectors $\mathbf{e}_\theta$ and $\mathbf{e}_\varphi$ are deflected into the polar unit vectors $\mathbf{e}_{\theta i}$ and $\mathbf{e}_{\varphi i}$ given by

$$\mathbf{e}_{\theta i} = \cos\theta_i \cos\varphi_i \mathbf{e}_{xi} + \cos\theta_i \sin\varphi_i \mathbf{e}_{yi} - \sin\theta_i \mathbf{e}_{zi}, \quad (47)$$

$$\mathbf{e}_{\varphi i} = -\sin\varphi_i \mathbf{e}_{xi} + \cos\varphi_i \mathbf{e}_{yi}, \quad (48)$$

where $(\mathbf{e}_{xi}, \mathbf{e}_{yi}, \mathbf{e}_{zi})$ are the Cartesian unit vectors in the global coordinate system $O_i x_i y_i z_i$ centred at the focal point of the detector lens. The transmitted field on the Gaussian reference sphere of the detector lens is then written as

$$\mathbf{E}_{si}(\theta_i, \varphi_i) = T_\theta E_{s\theta}(\theta_i, \varphi_i)\mathbf{e}_{\theta i} + T_\varphi E_{s\varphi}(\theta_i, \varphi_i)\mathbf{e}_{\varphi i}, \quad (49)$$

where $T_\theta = T_\theta(\theta_i, \varphi_i)$ and $T_\varphi = T_\varphi(\theta_i, \varphi_i)$ are the transmission coefficients (pupil function, apodization) for parallel and perpendicular polarization, respectively. Accumulated phase distortions, i.e. aberrations at the principal plane of the detector lens, as well as attenuations, i.e. amplitude factors, are integrated into the complex parameters T_θ and T_φ. The computation of T_θ and T_φ requires the knowledge of the imaging system and is based on the Fresnel equations. In our model, T_θ and T_φ are input parameters.

Step 3. In microscopy, the plane wave spectrum method is the essence of the Debye approximation and is often used for the calculation of the electromagnetic field near the focus of high numerical aperture objectives. However, for optical systems with high numerical aperture, this classical problem turns into a computational challenge due to the highly oscillatory behaviour of the involved functions. A novel and flexible implementation of the Debye integral incorporating the effects of amplitude, phase and polarization in an overall manner has been proposed in [18]. Instead of direct integration, the vector Debye diffraction integral is evaluated in the entire focal region with the fast Fourier transform. This implementation, which is used in our derivation, is summarized below.

In the Debye approximation, the transmitted field $\mathbf{E}_{si}$ as given by Equation (49) is the plane wave spectrum of the field $\mathbf{E}$ near the focus of the detector lens. Hence, the electric field $\mathbf{E}$ at a point (x_i, y_i, z_i) is obtained by integrating the propagating plane waves, i.e.

$$\mathbf{E}(x_i, y_i, z_i) = -j\frac{f_i}{\lambda_0}\int_0^{2\pi}\int_0^{\Theta_i} \mathbf{E}_{si}(\theta_i, \varphi_i) \times e^{j(k_{ix}x_i + k_{iy}y_i + k_{iz}z_i)} \sin\theta_i \, d\theta_i \, d\varphi_i, \quad (50)$$

where Θ_i is the aperture angle of the detector lens, and

$$k_{ix} = k_i \sin\theta_i \cos\varphi_i, \quad (51)$$

$$k_{iy} = k_i \sin\theta_i \sin\varphi_i, \quad (52)$$

$$k_{iz} = k_i \cos\theta_i, \quad (53)$$

with $k_i = k_0 n_i$. Using representations (51) and (52), we express the integral in Equation (50) as

$$\mathbf{E}(x_i, y_i, z_i) = -j\frac{f_i}{\lambda_0 k_i^2}\int_{D_k} \frac{\mathbf{E}_{si}(\theta_i, \varphi_i)}{\cos\theta_i} e^{jk_i z_i \cos\theta_i} \times e^{j(k_{ix}x_i + k_{iy}y_i)} dk_{ix} dk_{iy}, \quad (54)$$

with

$$D_k = \{(k_{ix}, k_{iy}) \mid \sqrt{k_{ix}^2 + k_{iy}^2} \le K\} \quad (55)$$

and $K = k_i \sin\Theta_i = k_0 \, \mathrm{NA}_i$. For an equidistant sampling $k_{ix} = m\Delta K$ and $k_{iy} = n\Delta K$, where $\Delta K = K/M$, M is the number of sampling points over K, and $m, n = -M, \ldots, M$, the sampling polar angles are

$$\theta_{imn} = \arcsin\left(\frac{\Delta K}{k_i}\sqrt{m^2 + n^2}\right), \quad (56)$$

$$\varphi_{imn} = \arccos\left(\frac{m}{\sqrt{m^2 + n^2}}\right), \quad (57)$$

and the numerical implementation of integral (54) is

$$\mathbf{E}(x_i, y_i, z_i) = -j\frac{f_i \Delta K^2}{\lambda_0 k_i^2}\sum_{m=-M}^{M}\sum_{n=-M}^{M} \frac{\mathbf{E}_{si}(\theta_{imn}, \varphi_{imn})}{\cos\theta_{imn}} \times e^{jk_i z_i \cos\theta_{imn}} e^{j\Delta K(mx_i + ny_i)}, \quad (58)$$

with

$$\mathbf{E}_{si}(\theta_{imn}, \varphi_{imn}) = 0 \quad \text{for } \sqrt{m^2 + n^2} > M.$$

A fast Fourier transform (FFT) is then used for computation of the double sum in Equation (58). For this purpose, we choose the number of FFT sampling points per transformed dimension $N = 2^s$, where s is an integer, such that the condition $N \ge 4M$ is satisfied. This condition can be explained as follows. Due to the Debye diffraction integral, the field $\mathbf{E}_{si}$ is the plane wave spectrum of the field $\mathbf{E}$, and usually, the smallest area (aperture matrix) containing $\mathbf{E}_{si} \neq 0$ is transformed. The spectral product $\exp(jk_{iz}z_i)\mathbf{E}_{si}/\cos\theta_i$ represents the spatial convolution $\mathcal{F}(\exp(jk_{iz}z_i)) \star \mathcal{F}(\mathbf{E}_{si}/\cos\theta_i)$, where $\mathcal{F}$ denotes the Fourier transform. In general, the result of the convolution is non-zero on an area larger than the aperture size, which may cause aliasing. Therefore, the aperture matrix is enlarged by zero padding to at least twice its dimensions ($N \ge 2(2M)$) before performing the transform. In a final step, simple cropping of the transform output removes the padding. Mathematically this process can be described as follows:

(1) for $m_1, n_1 = 0, \ldots, N-1$, compute the aperture matrix as

$$\mathbf{E}_{\mathrm{A}m_1n_1}(z_\mathrm{i}) = -\mathrm{j}\frac{f_\mathrm{i}\Delta K^2}{\lambda_0 k_\mathrm{i}^2}\frac{\mathbf{E}_\mathrm{si}(\theta_{\mathrm{im}_1-Mn_1-M}, \varphi_{\mathrm{im}_1-Mn_1-M})}{\cos\theta_{\mathrm{im}_1-Mn_1-M}} \times \mathrm{e}^{\mathrm{j}k_\mathrm{i}z_\mathrm{i}\cos\theta_{\mathrm{im}_1-Mn_1-M}},$$

with

$$\mathbf{E}_{\mathrm{A}m_1n_1}(z_\mathrm{i}) = 0 \text{ for } \sqrt{(m_1-M)^2+(n_1-M)^2} > M;$$

(2) compute the Fourier-transformed matrix

$$\mathbf{E}_{\mathrm{F}m_1n_1}(z_\mathrm{i}) = \mathcal{F}(\mathbf{E}_{\mathrm{A}m_1n_1}(z_\mathrm{i}));$$

(3) for $m_2, n_2 = -N/2+1, \ldots, N/2$, compute the focus field $\mathbf{E}$ at the sampling points $x_{\mathrm{im}_2} = m_2\Delta x$ and $y_{\mathrm{in}_2} = n_2\Delta y$ as

$$\mathbf{E}(x_{\mathrm{im}_2}, y_{\mathrm{im}_2}, z_\mathrm{i}) = \mathbf{E}_{\mathrm{F}m_2+N/2-1n_2+N/2-1}(z_\mathrm{i}),$$

where

$$\Delta x = \Delta y = \frac{2\pi}{N\Delta K}; \tag{59}$$

(4) crop the matrix $\mathbf{E}(x_{\mathrm{im}_2}, y_{\mathrm{im}_2}, z_\mathrm{i})$ by restricting m_2 and n_2 to vary in the range $m_2, n_2 = -N_\mathrm{c}/2+1, \ldots, N_\mathrm{c}/2$, where $N_\mathrm{c} < N$.

Along the z_i-direction, the sampling can be chosen arbitrarily by respecting the condition

$$M > \frac{2(\mathrm{NA_i})^2}{\sqrt{n_\mathrm{i}^2-(\mathrm{NA_i})^2}}\frac{|z_\mathrm{i}|}{\lambda_0}. \tag{60}$$

Condition (60) also known as the sampling condition guarantees that the propagation factor $\exp(\mathrm{j}k_\mathrm{i}z_\mathrm{i}\cos\theta_\mathrm{i})$ is calculated with high resolution. In particular, the phase term $k_\mathrm{i}z_\mathrm{i}\cos\theta_\mathrm{i}$ does not change by more than π between neighbouring sampling points in the Gaussian reference sphere. In addition, a lower limit of $M > 50$ was found to be necessary for an accurate sampling of φ_i. Deviations from these sampling conditions result in granular artefacts in the final computed image. As a typical value for M, we chose $M = 120$, while for the axial distance z_i, we impose $|z_\mathrm{i}| < 25\lambda_0$, corresponding to $|z_\mathrm{i}| < 16\,\mu$m at a wavelength of 635 nm. The final result is the distribution of the intensity

$$I_{m_2n_2}(z_\mathrm{i}) = |E_\mathrm{x}(x_{\mathrm{im}_2}, y_{\mathrm{im}_2}, z_\mathrm{i})|^2 + |E_\mathrm{y}(x_{\mathrm{im}_2}, y_{\mathrm{im}_2}, z_\mathrm{i})|^2 + |E_\mathrm{z}(x_{\mathrm{im}_2}, y_{\mathrm{im}_2}, z_\mathrm{i})|^2,$$

at the sampling points $(x_{\mathrm{im}_2} = m_2\Delta x, y_{\mathrm{in}_2} = n_2\Delta y)$ in the axial plane z_i.

3. Numerical simulations

In our numerical simulations, we choose the wavelength in free space $\lambda_0 = 0.635\,\mu$m , the refractive index in the object space (water) $n_\mathrm{o} = 1.33$, the refractive index of the particle $n_\mathrm{p} = 1.591$, the refractive index of the substrate (glass) $n_\mathrm{s} = 1.51$, the refractive index in the image space (water) $n_\mathrm{i} = 1.33$, the transversal magnification $m_\mathrm{T} = f_\mathrm{i}/f_\mathrm{o} = 60$, and the numerical aperture in the object space $\mathrm{NA_o} = 1.0$. The polarization angle of the incident wave is $\alpha_\mathrm{pol} = 45^\circ$.

First, we analyse the accuracy of the newly developed code devoted to the scattering analysis of axisymmetric particles with arbitrary orientation. For this purpose, we take the results obtained for a spherical particle as in [17]. In the new code, the spherical particle is treated as an axisymmetric particle, and the parameters of calculation are chosen as follows: $a = b = 1.0\,\mu$m, $\alpha_\mathrm{p} = 30^\circ$, $\beta_\mathrm{p} = 45^\circ$, and $\beta_\mathrm{s} = 45^\circ$. By this choice of the particle orientation angles (i.e. $\alpha_\mathrm{p} = 30^\circ$ and $\beta_\mathrm{p} = 45^\circ$), we check the correctness of the new implementation based on the rotation addition theorem. The results illustrated in Figure 2 show a complete agreement between the scattering curves.

In Figure 3, we show the focus intensity distribution along the x_i-axis for an axisymmetric particle with $a = 1.0\,\mu$m and $b = 0.5\,\mu$m. The original image $I_{m_2n_2}(0)$ with $N = 512$ is first cropped by considering the image $I_{m_2n_2}(0)$ with $N_\mathrm{c} = 128$, and then filtered out by setting $I_{m_2n_2}(0) = 0$ if $I_{m_2n_2}(0) < \varepsilon I_\mathrm{max}(0)$, where $I_\mathrm{max}(0) = \max_{m_2,n_2} I_{m_2n_2}(0)$ and $\varepsilon = 10^{-3}$. In this simulation and the subsequent ones, we choose $M = 120$, so that the condition $N > 4M$ is satisfied.

From our theoretical analysis, we know that if $\beta_\mathrm{s} < \beta_\mathrm{sc}$, the particle is illuminated by a propagating wave, while in the converse situation, namely when $\beta_\mathrm{s} > \beta_\mathrm{sc}$, the particle is illuminated by an evanescent wave. Note that for the scattering problem under examination, the critical angle of total internal reflection (after which evanescent waves appear) is

$$\beta_\mathrm{sc} = \arcsin\left(\frac{n_\mathrm{o}}{n_\mathrm{s}}\right) \approx 61.73^\circ.$$

In Figure 4, we illustrate the focus intensity distributions for a particle placed at an effective distance $d = 0.1\,\mu$m with respect to the plane surface, and being illuminated at two angles of incidence: $\beta_\mathrm{s} = 0^\circ < \beta_\mathrm{sc}$ and $\beta_\mathrm{s} = 62^\circ > \beta_\mathrm{sc}$. In the first case, the image of the particle has a good contrast, while in the second case, the image is blurry. In Table 1 we show the integral response of the same particle for three values of the incident angle β_s, and two values of the effective distance between the particle and the plane surface d. As it can be seen, for $\beta_\mathrm{s} < \beta_\mathrm{sc}$, the

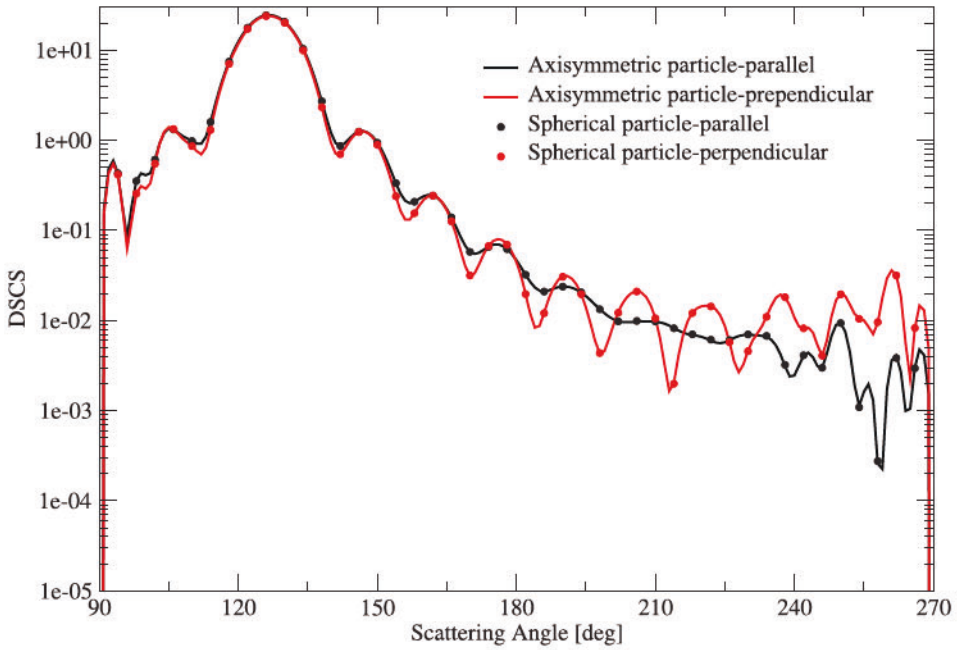

Figure 2. Differential scattering cross sections for parallel and perpendicular polarization of a homogeneous spherical particle with $a = b = 1\ \mu$m.

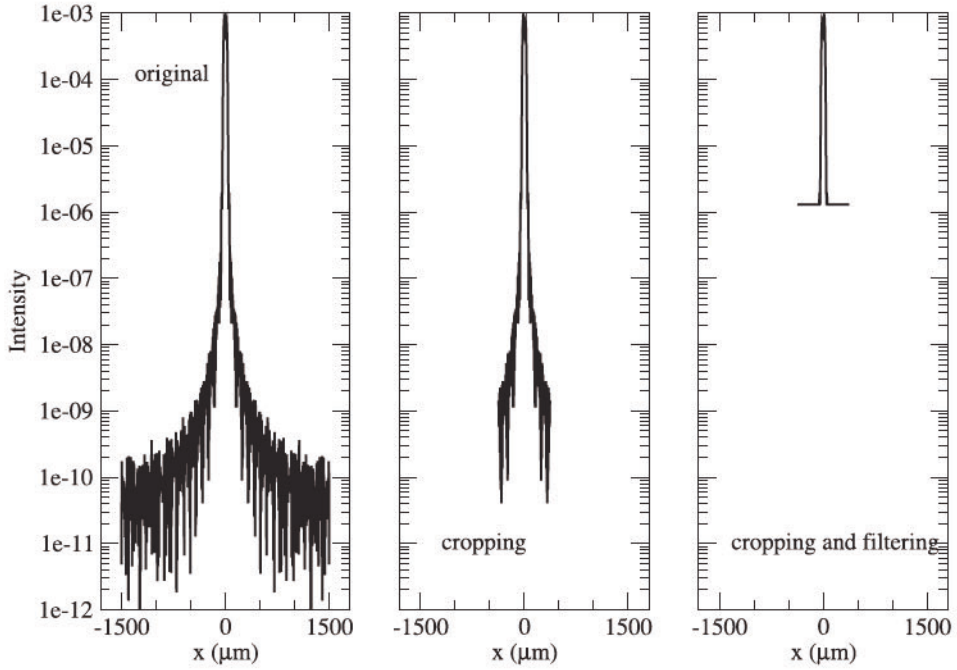

Figure 3. The focus intensity distribution along the x_I-axis. The original image is first cropped and then filtered.

integral response is insensitive with respect to d, while for $\beta_s > \beta_{sc}$, the integral response decreases by a factor of 5 when d increases from 0.1 μm to 1.0 μm.

The plots in Figures 5 and 6 confirm the above findings. For $\beta_s < \beta_{sc}$, the image in Figure 5, with an excellent quality in terms of sharpness and contrast, carries information on the size and the orientation of the particle, while for $\beta_s > \beta_{sc}$, the image in Figure 6 is blurry. However, in the second case, the integral response P plotted in Figure 7 contains information about the effective distance d. In fact, this combination of figures demonstrates an approach for determining the impact of collecting scattered light from an image [11,13], as is done with a digital camera. Experiments consist of collecting images similar to those shown in Figure 5 with subsequent integration, as is shown in Figure 7. Note, however,

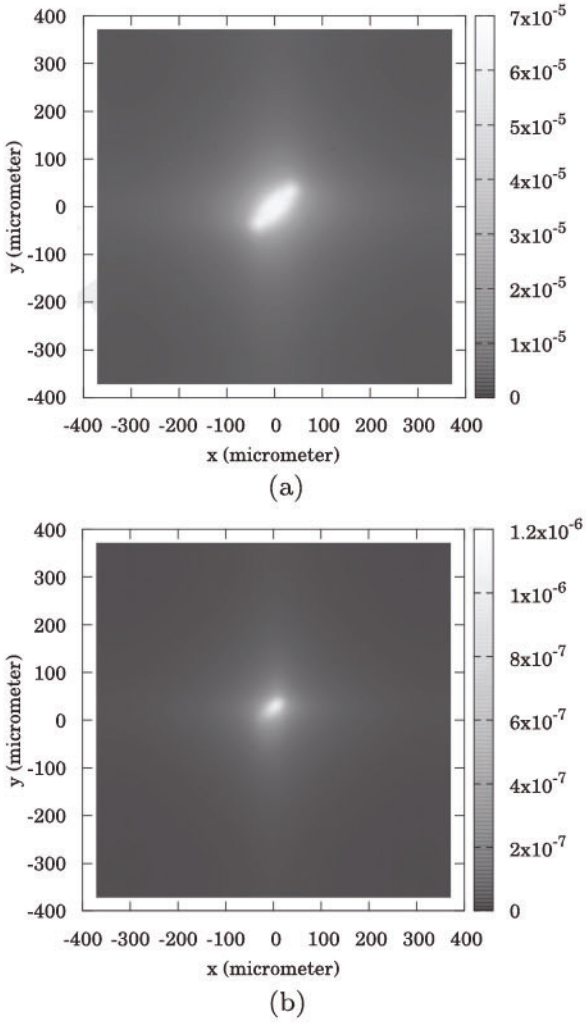

Figure 4. The focus intensity distributions for a particle with $a = 1.5\ \mu$m, $b = 0.5\ \mu$m, $\alpha_p = 45^\circ$, and $\beta_p = 90^\circ$. The incident angle is $\beta_s = 0^\circ$ (a) and $\beta_s = 62^\circ$ (b). The effective distance between the particle and the plane surface is $d = 0.1\ \mu$m.

Table 1. Integral response of a particle with $a = 1.5\ \mu$m, $b = 0.5\ \mu$m, $\alpha_p = 45^\circ$, and $\beta_p = 90^\circ$ for three values of the incident angle β_s, and two values of the effective distance between the particle and the plane surface d.

β_s	$d = 0.1\ \mu$m	$d = 1.0\ \mu$m
0°	1.07E+03	1.07E+03
45°	3.53E+02	3.52E+02
62°	4.08E+00	7.5E−01

that the influence of the camera itself has not been included.

Referring again to Figure 7, a rough estimate can be made: if P can be measured with a resolution of $1/\Delta P$, where $\Delta P = P_{\max} - P_{\min} \approx 2.8$, then d can be measured with a resolution of about 10 nm. Moreover, it is apparent that the integral response decays exponentially with the distance. Fitting the model data with the exponential curve $P(d = 0)\exp(-d/\rho)$, we found that the decay

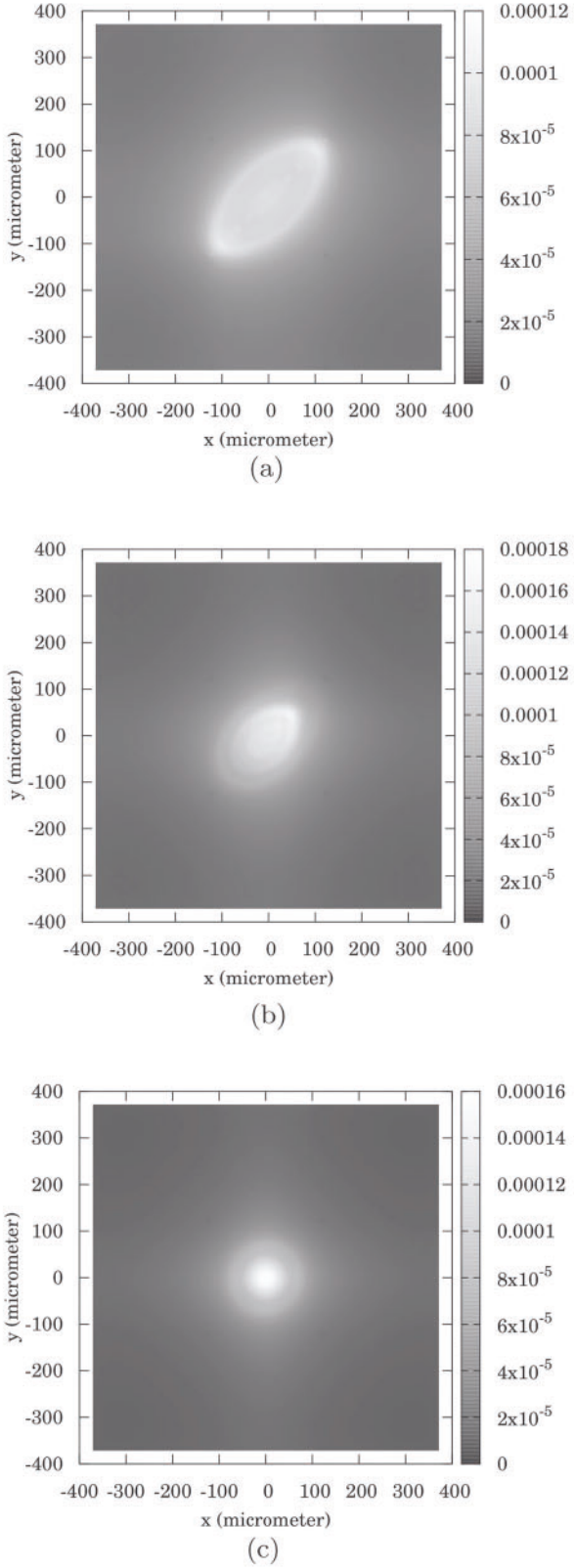

Figure 5. The focus intensity distribution for a particle with $a = 3.0\ \mu$m and $b = 1.5\ \mu$m. The incident angle is $\beta_s = 0^\circ$, and the effective distance between the particle and the plane surface is $d = 0.1\ \mu$m. The azimuth orientation angle of the particle is $\alpha_p = 45^\circ$, while the zenith orientation angle are $\beta_p = 90^\circ$ (a), $\beta_p = 45^\circ$ (b), and $\beta_p = 0^\circ$ (c).

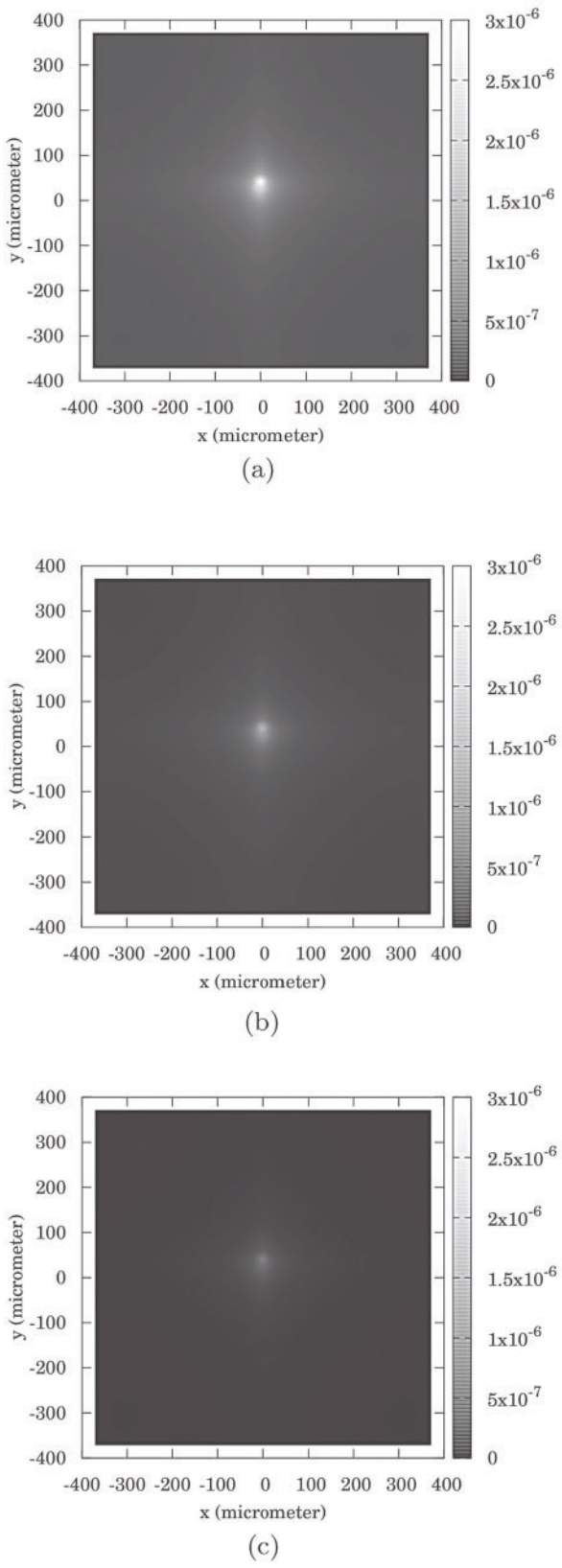

Figure 6. The focus intensity distributions for a particle with $a = 2.0\,\mu$m, $b = 1.0\,\mu$m, $\alpha_p = 45^\circ$, and $\beta_p = 90^\circ$. The incident angle is $\beta_s = 62^\circ$, and the effective distance between the particle and the plane surface is $d = 0.1\mu$m (a), $d = 0.5\mu$m (b), and $d = 1.0\,\mu$m (c).

length is $\rho = 0.55\,\mu$m . This value is very close to the penetration depth of the evanescent wave ρ_0, estimated as [19]

$$\rho_0 = \frac{\lambda_0}{4\pi\sqrt{(n_s \sin\beta_s)^2 - n_o^2}} \approx 0.543\,\mu\text{m}. \qquad (61)$$

Experimental application of the model to TIRM will require an apparatus utilizing a digital camera, rather than a photomultiplier tube. The camera will capture images of the morphology of evanescent wave scattering from a particle. As shown above, the scattering morphology contains information related to the separation distance, orientation, and shape of the particle. Morphology mapping simulations will be paired with experiments, in which images of scattering from particles of known orientation, separation distance, and shape will be obtained. These maps will provide not only experimental verification of the model, but also a reference, either via direct comparison or analytical expression, for the measurement of a particle of unknown orientation and separation distance. Previous work has shown how to subsequently assemble a potential energy landscape from these separation distance and orientation observations [20]. We suggest the name for the technique, where scattering morphology (instead of the integrated intensity) is used to calculate particle position and orientation, as 'Scattering Morphology Resolved Total Internal Reflection Microscopy (SMR – TIRM)'.

4. Conclusions

In this paper, a light scattering model for TIRM is described. The model deals with scattering by an axisymmetric particle of arbitrary orientation situated near a plane surface, and imaging of the scattered light. Scattering by an axisymmetric particle of arbitrary orientation situated near a plane surface is analysed by using the T-matrix method and the rotation addition theorem for spherical vector wave functions. Essentially, this theorem enabled us to pass from the field expansions in the global coordinate system to the field expansions in the particle coordinate system and vice versa. A direct consequence of the arbitrary particle orientation is that the scattering problem does not decouple over the azimuthal modes as it happens when the axis of symmetry of the particle is perpendicular to the plane surface. The computation of the image of the scattered field has been performed in three steps: (i) computation of the scattered field on the Gaussian reference sphere of the collector lens, (ii) computation of the transmitted field on the Gaussian reference sphere of the detector lens, and (iii) computation of the focus field by means of the Debye diffraction integral.

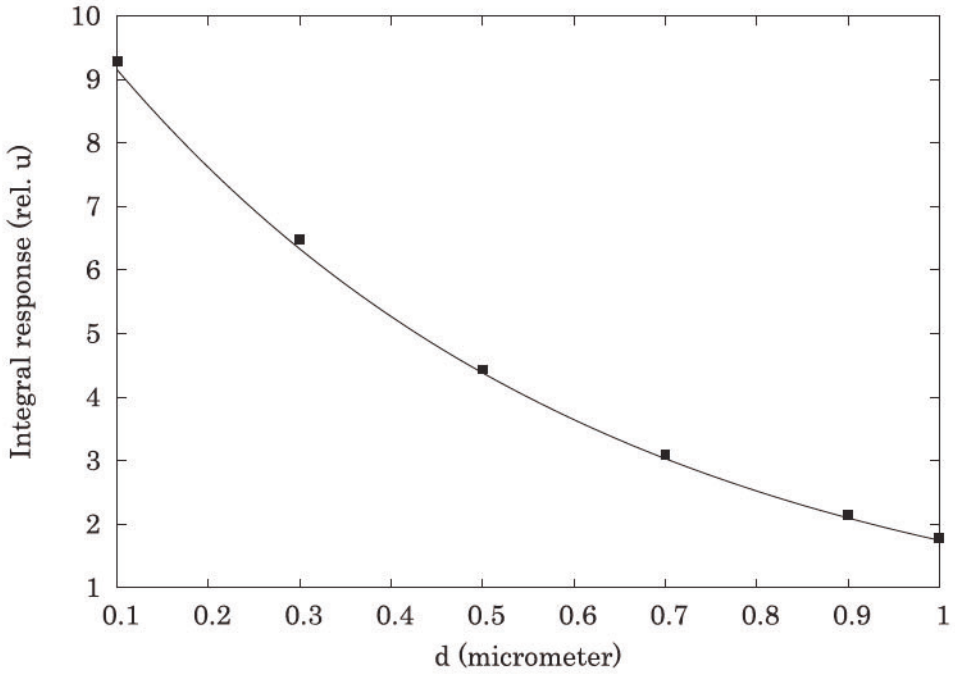

Figure 7. Integral response of the same particle as in Figure 6 as a function of the effective distance between the particle and the plane surface *d*. The solid curve is the exponential function fitted to the data (dots).

Our numerical simulations indicated that two working regimes for TIRM can be identified.

(1) The first regime, corresponding to an incident angle less than the critical angle of total internal reflection, provides information on the size and the orientation of the particle; the computed images have a good contrast, and the particle shape is clearly visualized.
(2) The second regime, corresponding to an incident angle larger than the critical angle of total internal reflection, is recommended for measuring the effective distance between the particle and plane surface. As a matter of fact, it seems that TIRM offers the possibility to measure effective distances with a resolution of 10 nm.

Disclosure statement

No potential conflict of interest was reported by the authors.

Funding

Christopher L. Wirth was supported by the National Science Foundation CAREER Award no. 1752051.

References

(1) Prieve D.C.; Luo F.; Lanni F. Brownian Motion of a Hydrosol Particle in a Colloidal Force Field. *Faraday Discuss. Chem. Soc.* [Online] **1987**, *83*, 297. https://doi.org/10.1039/dc9878300297.
(2) von Grünberg H.H.; Helden L.; Leiderer P.; Bechinger C. Measurement of Surface Charge Densities on Brownian Particles Using Total Internal Reflection Microscopy. *J. Chem. Phys.* [Online] **2001**, *114* (22), 10094–10104. https://doi.org/10.1063/1.1371556.
(3) Prieve D.C.; Hoggard J.D.; Fu R.; Sides P.J.; Bethea R. Two Independent Measurements of Debye Lengths in Doped Nonpolar Liquids†. *Langmuir* [Online] **2008**, *24* (4), 1120–1132. https://doi.org/10.1021/la702351e.
(4) Bevan M.A.; Prieve D.C. Direct Measurement of Retarded van der Waals Attraction. *Langmuir* [Online] **1999**, *15* (23), 7925–7936. https://doi.org/10.1021/la981381l.
(5) Helden L.; Dietrich K.; Bechinger C. Interactions of Colloidal Particles and Droplets with Water–Oil Interfaces Measured by Total Internal Reflection Microscopy. *Langmuir* [Online] **2016**, *32* (51), 13752–13758. https://doi.org/10.1021/acs.langmuir.6b03864.
(6) Fagan J.A.; Sides P.J.; Prieve D.C. Evidence of Multiple Electrohydrodynamic Forces Acting on a Colloidal Particle near an Electrode Due to an Alternating Current Electric Field. *Langmuir* [Online] **2005**, *21* (5), 1784–1794. https://doi.org/10.1021/la048076m.
(7) Wirth C.L.; Sides P.J.; Prieve D.C. The Imaging Ammeter. *J. Colloid Interface Sci.* [Online] **2011**, *357* (1), 1–12. https://doi.org/10.1016/j.jcis.2011.01.025.
(8) Bevan M.A.; Prieve D.C. Forces and Hydrodynamic Interactions Between Polystyrene Surfaces with Adsorbed PEO-PPO-PEO. *Langmuir* [Online] **2000**, *16* (24), 9274–9281. https://doi.org/10.1021/la0006869.
(9) Beltran-Villegas D.J.; Edwards T.D.; Bevan M.A. Self-Consistent Colloidal Energy and Diffusivity Landscapes in Macromolecular Solutions. *Langmuir* [Online] **2013**, *29* (40), 12337–12341. https://doi.org/10.1021/la403261m.

(10) Kleshchanok D.; Tuinier R.; Lang P.R. Depletion Interaction Mediated by a Polydisperse Polymer Studied with Total Internal Reflection Microscopy. *Langmuir* [Online] **2006**, *22* (22), 9121–9128. https://doi.org/10.1021/la061657m.

(11) Biggs S.; Dagastine R.R.; Prieve D.C. Oscillatory Packing and Depletion of Polyelectrolyte Molecules at an Oxide-Water Interface. *J. Phys. Chem. B* [Online] **2002**, *106* (44), 11557–11564. https://doi.org/10.1021/jp026425k.

(12) Bike S.G. Measuring Colloidal Forces Using Evanescent Wave Scattering. *Curr. Opin. Colloid Interface Sci.* [Online] **2000**, *5* (1–2), 144–150. https://doi.org/10.1016/s1359-0294(00)00047-9.

(13) Bevan M.A.; Eichmann S.L. Optical Microscopy Measurements of kT-Scale Colloidal Interactions. *Curr. Opin. Colloid Interface Sci.* [Online] **2011**, *16* (2), 149–157. https://doi.org/10.1016/j.cocis.2010.12.006.

(14) Helden L.; Eremina E.; Riefler N.; Hertlein C.; Bechinger C.; Eremin Y.; Wriedt T. Single-Particle Evanescent Light Scattering Simulations for Total Internal Reflection Microscopy. *Appl. Opt.* [Online] **2006**, *45* (28), 7299. https://doi.org/10.1364/ao.45.007299.

(15) Hertlein C.; Riefler N.; Eremina E.; Wriedt T.; Eremin Y.; Helden L.; Bechinger C. Experimental Verification of an Exact Evanescent Light Scattering Model for TIRM. *Langmuir* [Online] **2008**, *24* (1), 1–4. https://doi.org/10.1021/la703322d.

(16) Stein S. Addition Theorem for Spherical Wave Functions. *Q. Appl. Math.* [Online] **1961**, *19* (1), 15–24. http://www.jstor.org/stable/43634833.

(17) Doicu A.; Wriedt T.; Eremin Y.A. *Light Scattering by Systems of Particles* [Online]; Springer: Berlin, Heidelberg, **2006**. https://doi.org/10.1007/978-3-540-33697-6.

(18) Leutenegger M.; Rao R.; Leitgeb R.A.; Lasser T. Fast Focus Field Calculations. *Opt. Express* [Online] **2006**, *14* (23), 11277–11291. https://doi.org/10.1364/oe.14.011277.

(19) McKee C.T.; Clark S.C.; Walz J.Y.; Ducker W.A. Relationship between Scattered Intensity and Separation for Particles in an Evanescent Field. *Langmuir* [Online] **2005**, *21* (13), 5783–5789. https://doi.org/10.1021/la046856p.

(20) Rashidi A.; Wirth C.L. Motion of a Janus Particle Very Near a Wall. *J. Chem. Phys.* [Online] **2017**, *147* (22), 224906. https://doi.org/10.1063/1.4994843.